Recurrent Filmwise and Dropwise Condensation on a Beetle Mimetic Surface

Youmin Hou,[†] Miao Yu,[‡] Xuemei Chen,[§] Zuankai Wang,[*,§] and Shuhuai Yao[*,†,‡]

[†]Department of Mechanical and Aerospace Engineering, The Hong Kong University of Science and Technology, Kowloon, Hong Kong, [‡]Bioengineering Graduate Program, The Hong Kong University of Science and Technology, Kowloon, Hong Kong, and [§]Department of Mechanical and Biomedical Engineering, City University of Hong Kong, Kowloon, Hong Kong

ABSTRACT Vapor condensation plays a key role in a wide range of industrial applications including power generation, thermal management, water harvesting and desalination. Fast droplet nucleation and efficient droplet departure as well as low interfacial thermal resistance are important factors that determine the thermal performances of condensation; however, these properties have conflicting requirements on the structural roughness and surface chemistry of the condensing surface or condensation modes (*e.g.*, filmwise *vs* dropwise). Despite intensive efforts over the past few decades, almost all studies have focused on the dropwise condensation enabled by superhydrophobic surfaces. In this work, we report the development of a bioinspired hybrid surface with high wetting contrast that allows for seamless integration of filmwise and dropwise condensation modes. We show that the synergistic cooperation in the observed recurrent condensation modes leads to improvements in all aspects of heat transfer properties including droplet nucleation density, growth rate, and self-removal, as well as overall heat transfer coefficient. Moreover, we propose an analytical model to optimize the surface morphological features for dramatic heat transfer enhancement.

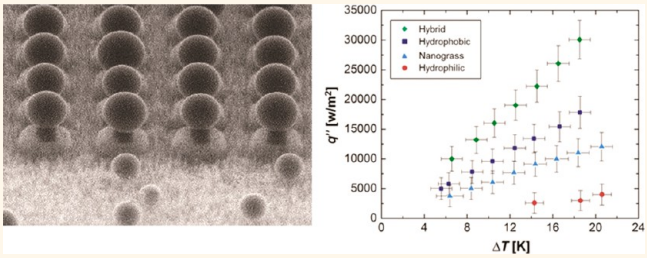

KEYWORDS: filmwise condensation · dropwise condensation · nanostructure · heterogeneous wettability · heat transfer enhancement

Vapor condensation takes place in various industrial applications including thermal management,[1,2] power generation,[3] water desalination,[4,5] and water harvesting systems.[6−8] In all of these applications, an efficient condensation process is desired to improve energy efficiency, security and environmental protection. Typically, condensation is highly dependent on the physiochemical properties of the condenser surface. On a hydrophilic surface, condensation is characterized by the formation of an accumulative liquid film which is immobile. Such termed filmwise condensation is plagued with low heat transfer coefficient despite the preference of the initial nucleation. In striking contrast to filmwise condensation, dropwise condensation that takes place on nonwettable surfaces promises a significant increase in heat and mass transfer performance,[9] since the isolated condensed droplets on such surfaces can be easily removed. Furthermore, on judiciously designed superhydrophobic surfaces, the droplet mobility can be significantly improved. Because of the minimal contact line pinning of the condensed droplets in the Cassie or partial-wetting state on rough nanostructures,[10−14] these droplets can be self-propelled from the surface at a typical radius of 10−100 μm, which is 2 orders of magnitude smaller than the gravity-driven droplets on unstructured hydrophobic surfaces.[15−20] Over the past decade, various artificial surfaces have been developed to enhance the condensation heat transfer.[21−35] To our best knowledge, almost all efforts have focused on design of robust superhydrophobic surfaces working in the regime of dropwise condensation. Recently, Miljkovic *et al.* elegantly demonstrated that a superhydrophobic nanostructured copper surface resulted in 30% enhancement in heat transfer coefficient compared to the flat hydrophobic surface at low supersaturations (<1.12).[23] Although

* Address correspondence to meshyao@ust.hk, zuanwang@cityu.edu.hk.

Received for review October 8, 2014 and accepted December 7, 2014.

Published online December 07, 2014
10.1021/nn505716b

the superhydrophobic surface allows for sustained dropwise condensation, it is susceptible to a number of issues. First, since the nucleation energy barrier on a superhydrophobic surface is much higher than that on a hydrophilic surface, the droplet nucleation density on the superhydrophobic surface is severely reduced compared to that on the hydrophilic surface, especially in the early stage of nucleation.[36−38] Second, although the presence of the vapor layer within the superhydrophobic nanostructures enables the condensate droplets to stay in the Cassie state, the vapor layer also causes an additional thermal resistance.[39] Third, due to the Laplace pressure instability mechanism,[12,40−44] the condensed droplets tend to transition from the suspended Cassie state to the unwanted sticky Wenzel state,[45−48] which highly affects the droplet departure efficiency. In addition, under the high supersaturation conditions, the increased droplet nucleation density induces liquid flooding within the nanostructures and the collapse of dropwise condensation.[23,26,46] Thus, an efficient condensation surface that enables increased droplet nucleation density,[49] reduced droplet departure size,[37,50] and minimal thermal barrier[39,51] demands a synergistic cooperation of these advantages inherent in both modes of dropwise and filmwise condensation simultaneously. However, since these two condensation modes have distinctly conflicting requirements on the surface wettability and architecture, it has, to date, remained extremely challenging to develop a robust surface that can reinforce both filmwise and dropwise condensation processes for enhanced heat transfer.[38,52]

Inspired by the Namib dessert beetle, which utilizes its bumpy back with hydrophilic and hydrophobic patches to condense and collect water droplets,[53] as well as the recent efforts in heterogeneous condensation and freezing,[28,29,38,54] here we propose a hybrid surface with patterned high-contrast wettability to achieve enhanced condensation heat transfer. Distinctive from the previous studies,[28,52] by confining the hydrophilic patches on the top of the micropillars which are surrounded by superhydrophobic nanograss, such a novel hybrid surface enables not only higher density nucleation, but also droplet depinning on the extreme hydrophilic area. Particularly, the unique morphological and wetting features achieve a natural recurrent transition from filmwise-to-dropwise condensation which has not been reported before. This novel design provides an effective approach for enhancing water nucleation as well as self-propelled departure, which reconciles the conflicting requirements for desired condensation heat transfer. By systematically conducting experiments in both environmental scanning electron microscopy (ESEM) and ambient conditions with controlled humidity, we demonstrated that the droplet nucleation density and the initial droplet growth rate on the hybrid surface were both much higher than that of the superhydrophobic surfaces with no hydrophilic patterns.[38] According to the thermal characterization, the novel hybrid surface showed ~63% enhancement in heat transfer coefficient as compared to the flat hydrophobic surface. This work reveals the undiscovered impact of heterogeneous wettability and architectures on the microdroplets morphology transition, and provides an avenue *via* designing high-contrast wettability patterns to improve the performance of condensation heat transfer.

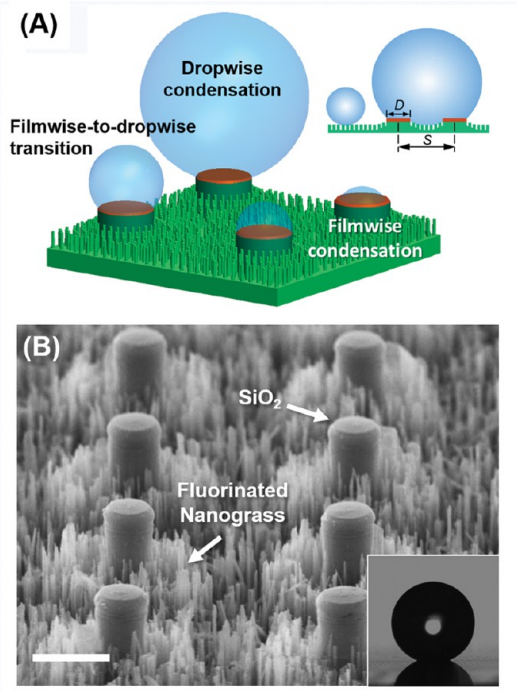

Figure 1. Design of the hybrid surface with high wetting contrast. (A) Schematics of the hybrid surface showing the heterogeneous wettability. The top of the micropillar (dark red area) is hydrophilic, which is energetically favored for droplet nucleation and growth. A hydrophobic layer is selectively coated on the nanograss (green area), providing a global superhydrophobicity for dropwise condensation. The right schematic shows a single droplet staying in the Cassie and hybrid-wetting state. (B) SEM image of the hybrid nanostructured silicon surface consisting of micropillar arrays and surrounding nanograss. Scale bar, 10 μm. The inset shows the contact angle of the hybrid surface is 161 $\pm$ 4°.

RESULTS

By leveraging the dependence of wettability on the surface roughness and chemistry, the hybrid surface is designed with a multiscale roughness and heterogeneous wettability. Figure 1A,B shows the schematic and scanning electron microscopy (SEM) images of the novel hybrid surface. The surface consists of patterned micropillar arrays. The tops of the micropillars are covered by hydrophilic silicon dioxide (SiO_2) to facilitate the filmwise condensation, *i.e.*, fast droplet nucleation and initial growth,[55] while the valleys between the micropillars are covered by conformal nanograss to promote the dropwise condensation (with coalescence-induced droplet self-removal). Moreover, by judiciously controlling the fraction of the hydrophilic SiO_2 patches

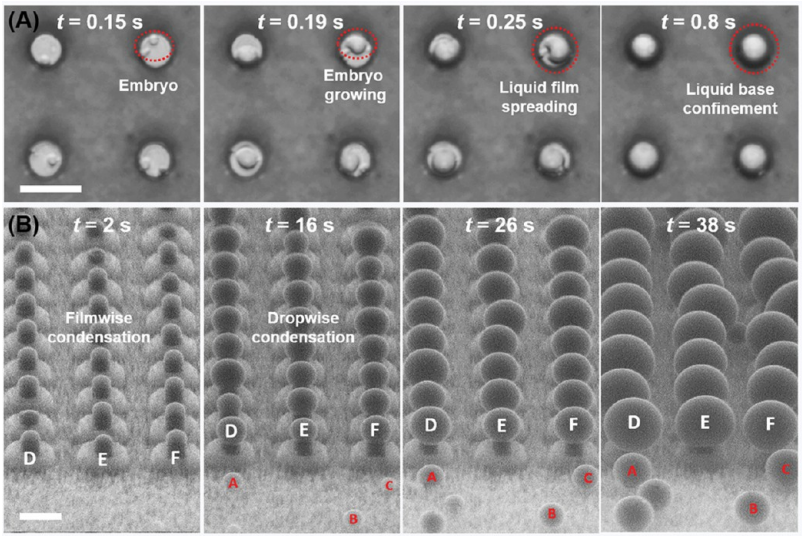

Figure 2. Combined filmwise and dropwise condensation. (A) Selected time-lapse images of water vapor condensation in the custom-made chamber. The snapshots show the filmwise condensation dynamics on the hydrophilic tops of the hybrid surface. Here, *D* and *S* are 6 and 18 μm, respectively. The vapor pressure in the experiment was 1930 $\pm$ 124 Pa, and the cooling stage temperature was 7.46 $\pm$ 0.55 °C. (B) Selected time-lapse images of water vapor condensation captured *via* ESEM. Scale bar, 10 μm. The droplets (*e.g.*, A, B, C) on the nanograss grow in the CCA mode, while droplets (*e.g.*, D, E, F) on the hybrid surface grow in the CCL mode. The distinct morphology of CCL droplets demonstrates the condensation transition from the filmwise mode to dropwise mode. The vapor pressure in ESEM chamber was 653 $\pm$ 13 Pa and the cooling stage temperature was 0.3 $\pm$ 0.2 °C.

across the whole surface, a recurrent condensation mode transition from the filmwise to the dropwise can be achieved. As shown in the SEM image, the diameter *D* and center-to-center spacing *S* of the micropillar on the hybrid surface are 6 and 24 μm, respectively. Between the micropillars lies the nanograss with ~200 nm in diameter, ~5 μm in height, and ~400−800 nm in pitch. For the surface fabrication, we first fabricated the SiO_2 patterns on the silicon wafer using standard photolithography and oxide etching processes. Then, micropillars with SiO_2 tops were etched using tetramethylammonium hydroxide (TMAH), and a modified deep reactive ion etching (DRIE) process was further implemented to form the nanograss covering the valleys of the micropillar arrays. To achieve the desired wetting contrast, the as-fabricated surface was conformally coated by a thin hydrophobic layer using a fluorination process and then buffered oxide etching (BOE) was used to selectively remove the superficial layers of SiO_2 and the fluoride polymer coating on the top of the micropillars, thereby recovering the hydrophilicity of the SiO_2 patterns (see details in Methods). The extreme wetting contrast on such a hybrid surface was verified by the Energy-Dispersive X-ray Spectroscopy (EDX) measurement of chemical composition on the surface (see Supporting Information Note 1). The wetting properties of corresponding materials with different wettability were characterized by the goniometric measurements (see Supporting Information Table S2). The advancing contact angles on flat SiO_2 and fluorinated nanograssed surfaces are 24.6 $\pm$ 5.2° and 167.1 $\pm$ 2.7°, respectively. By comparison, the apparent contact angle on the hybrid surface is 161.5 $\pm$ 4° (inset of Figure 1B), indicating a global superhydrophobicity on the hybrid surface despite the presence of abundant hydrophilic patches.

Combined Filmwise and Dropwise Condensation on the Hybrid Surface. To illustrate the combined condensation modes for preferential nucleation and rapid droplet growth, we first visualized the initial filmwise condensation of water vapor on the hybrid surfaces in a custom-made chamber (see Methods). The vapor pressure P_v was 1930 $\pm$ 124 Pa and the cooling stage temperature T_{stage} was 7.46 $\pm$ 0.55 °C. As shown in Figure 2A, during the condensation, the embryos preferentially nucleate on the hydrophilic patches, quickly grow and spread across the whole patches as a thin film, suggesting the signature of filmwise condensation (see Supporting Information Movie 1). To visualize the three-dimensional morphologies of the condensed droplets with high spatial resolution, we further conducted the condensation experiment in ESEM. The vapor pressure in the ESEM chamber P_v was 653 $\pm$ 13 Pa and the cooling stage temperature T_{stage} was 0.3 $\pm$ 0.2 °C (see Methods for details). We found that almost all the embryos started on the hydrophilic tops of the micropillars, revealing the spatial control of nucleation (see Supporting Information Movie 2). On the nanograss, the condensation was dominated by the heterogeneous nucleation, as shown by random droplets (*e.g.*, A, B, C, indicated in Figure 2B). Droplets growing on the nanograss maintained a constant contact angle (CCA) in a suspended state on the top of the nanograss.[39] Obviously, the nucleation density and growth rate were much lower than those on the hybrid surface.

Note that the filmwise condensation in our hybrid surface is different from that on the conventional

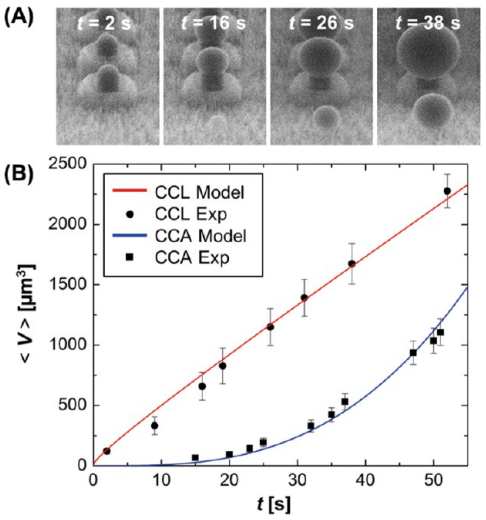

Figure 3. Droplet growth process and corresponding thermal analysis. (A) Selected time lapse ESEM images of CCL and CCA droplets showing the difference in the growth dynamics and rate. (B) Time evolution of the average droplet volume *V* of CCL and CCA droplets. The lines show the theoretical calculated droplet volume growth, for different modes, as a function of condensation time *t* (see Supporting Information Note 2). The filled circles and squares indicate the experimental data on different surfaces obtained in ESEM. For the CCL droplet, at the early stage, the rapid growth in the filmwise mode results from the lower thermal resistance between the droplet base and substrate. For the CCA droplet, the slower growth rate is due to the small initial contact base and the gas-filled nanogaps between the droplet and substrate.

hydrophilic surface, which is characterized by a liquid film spreading over the entire surface. Because of the spatial control in the droplet nucleation, the condensate droplets were confined on the top of tiny micropillars and displayed a constant contact line (CCL) growth mode with CA increasing over time. As the water volume increased with time, the localized liquid film gradually transitioned to isolated spherical droplets (*e.g.*, D, E, F, indicated in Figure 2B). This filmwise to dropwise transition can be attributed to the unique morphological and wetting features of our surface. It is important to point out that without the wetting contrast between the localized hydrophilic patches and surrounding nanograss, the condensate droplets tend to accumulate and eventually merge into a liquid film.[56−58]

On the basis of the experimental data from ESEM observation, the time evolutions of the droplet volume (V) for CCL and CCA droplets are shown in Figure 3. Here, we collected the data of droplet growth with varying starting times. The growth periods were normalized with respect to the droplet size for the CCL and CCA modes.[23] To investigate the droplet growth dependence on different modes, we modeled the growing process of a single droplet on the hybrid and nanograssed surfaces, respectively (see Supporting Information Note 2).[16,39,59] The modeling results (lines) in Figure 3 are in excellent agreement with the experimental data (symbols). The growth rate of the CCL droplet is initially much higher than that of the CCA droplet, and later becomes more closely aligned. On the basis of the measured single droplet growth before coalescence, we compared the droplet growth rate to the classical model $r = \rho t^{\alpha}$ for both modes.[6,34] For the CCA droplet on the nanograss, the α_{CCA} maintains at $\sim 0.53 \pm 0.04$, whereas in the case of the CCL droplet, the power law model fails to describe the droplet growth dynamics on the hybrid surface, suggesting that the growth mechanism on the hybrid patterns differs from that on the nanograss. At the early condensation stage ($V < 1000\ \mu m^3$), the CCL droplet on the hybrid surface exhibits at least 2.5 times faster in growth rate than the CCA droplet on the nanograssed surface. The divergent droplet volume increment of the two modes can be attributed to the different wetting morphologies that dominate the total thermal resistance of condensation heat transfer in the initial stage. For the CCA droplet suspended on the nanograss, the apparent contact angle is much larger than that of the liquid film in the CCL mode, resulting in a much higher droplet conduction resistance. Moreover, the trapped gas in the nanostructures and small liquid−solid contact area increase the interfacial thermal resistance, therefore further limiting the CCA droplet growth. In comparison, the CCL droplets on the hybrid surface grow much faster because the condensate starts as a liquid film that covers the entire hydrophilic top, providing a larger liquid−solid contact area with small contact angle for heat transfer. At the later stage of growth ($V > 1000\ \mu m^3$) when the condensate on the hybrid surface transitions from filmwise to dropwise, the growth rates of the droplets on the hybrid and nanograssed surfaces gradually become closer. This is because as the droplet gets larger in size, the thermal conduction resistance of the droplet begins to dominate the heat transfer, and the total thermal resistances in both modes become comparable. Meanwhile, the continuously increasing droplet basal area of the CCA droplet also contributes to the apparent rise of the growth rate.

Coalescence-Induced Droplet Departure. Remarkably, we observed that the filmwise to dropwise transition on the hybrid surface can activate an unusual coalescence-induced droplet departure,[11,60−62] and further promote the droplet self-removal efficiency. Conventionally, the liquid film condensed on a hydrophilic surface is susceptible to a large pinning force. For the hybrid surface, however, the liquid film nucleated on the patterned hydrophilic region rapidly grows and reaches a metastable spherical shape[63,64] due to the fact that the condensates are spatially confined in a tiny region and suspended by the surrounding superhydrophobic nanograss (see Supporting Information Note 3). When the adjacent metastable droplets coalesce with each other, sufficient surface energy is released to overcome the adhesion on the hybrid patterns, naturally resulting in a droplet self-propelling (Figure 4, also see Supporting Information Movies 3

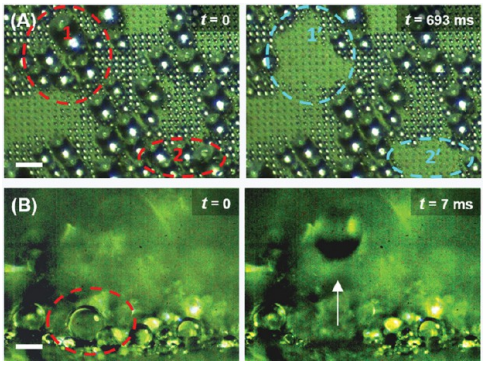

Figure 4. Droplet departure behaviors. Snapshots showing spontaneous droplet jumping: (A) top view (scale bar, 80 μm) and (B) side view (scale bar, 80 μm). All the images were acquired using a high speed camera. Along with volume increment, the transition from filmwise to dropwise condensation promises enough driven energy to overcome the contact pinning for droplet self-departure on the hybrid surface. The red dash circle denotes a group of droplets just prior to the coalescence and subsequent jumping, and the blue dash circle highlights the fresh space right after coalescence-induced jumping. The white arrow shows the droplet jumping trajectory. The vapor pressure in the experiment was 2800 $\pm$ 146 Pa, and the cooling stage temperature was 12.02 $\pm$ 0.38 °C.

and 4). Figure 4A shows the top view of droplet departure from the hybrid surface (D = 6 μm, S = 18 μm) in a custom-made chamber. As the metastable droplets interact with the adjacent droplets, a serial departure is triggered by coalescence, sweeping many mobile droplets off the surface.[47] This sweeping motion was captured as an out-of-plane motion, as shown in Figure 4B. As a result, many fresh dry areas were exposed for a continuous condensation process of renucleation and departure. During the coalescence process, we found that several droplets contacted both hydrophilic and superhydrophobic areas and formed a hybrid-wetting morphology. This natural evolution of hybrid-wetting status decreases the droplet adhesion by covering the nanograss and preserves the heat conduction path of the hydrophilic patterns as well. As a result, these droplets maintain a metastable state and tend to be more easily propelled by coalescence than the droplet on a single micropillar (see details in Supporting Information Note 3).

To gain a quantitative understanding, we characterized the condensation dynamics on hybrid surfaces with three different morphologies and the nanograssed surfaces. For the hybrid surfaces, we keep a constant D = 6 μm and vary the S from 12 to 24 μm, corresponding to S/D = 2, 3, 4. The droplet number density in the field of view (~300 μm × ~600 μm) for these four samples increased from ~(1.13 $\pm$ 0.15) × 10^9 m^{-2} for the nanograssed surface to (3.34 $\pm$ 0.11) × 10^9 m^{-2} for the hybrid surface with S/D = 2 (~196% increase), as shown in Figure 5A. Figure 5B shows the cumulative droplet departure volumes in the field of view (~1 mm × ~2 mm) for these four samples which

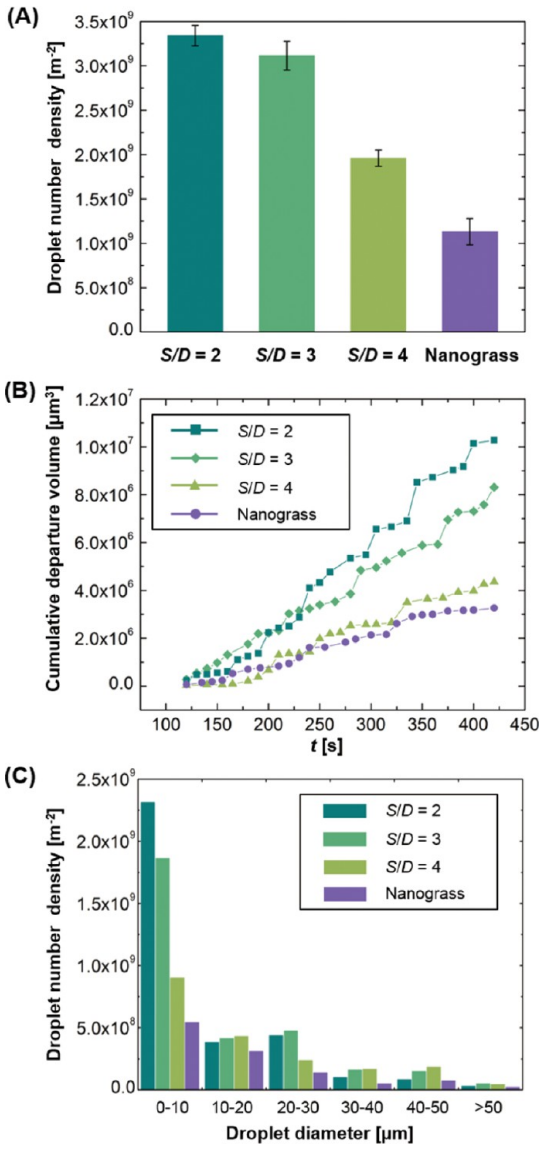

Figure 5. Characterization of condensation dynamics. (A) Measured overall droplet number density on the various surfaces showing the enhanced droplet nucleation *via* hydrophilic patterns. Error bars are from multiple measurements at different areas of the same sample. (B) Quantification of the cumulative droplet departure volumes on four different surfaces in 5 min condensation. For S/D = 2, the hybrid surface exhibits ~215% enhancement in the departure volume relative to the nanograssed surface. (C) Histogram of droplet size distribution, averaged for an interval of 5 min of condensation, on four different surfaces. The hybrid surface of S/D = 2 demonstrates a ~328% increase in droplets of <10 μm in diameter, compared to the nanograssed surface. The vapor pressure in the experiment was 2800 $\pm$ 146 Pa, and the cooling stage temperature was 12.02 $\pm$ 0.38 °C.

demonstrates a similar tendency. Compared to the nanograssed surface, nearly 215% increase in the cumulative droplet departure volume was achieved for the hybrid surface with S/D = 2. The droplet counts were averaged over all the images recorded during a 5 min period of condensation, while droplet departure volume was estimated from the departed droplets by comparing sequential images taken at ~12 s intervals.

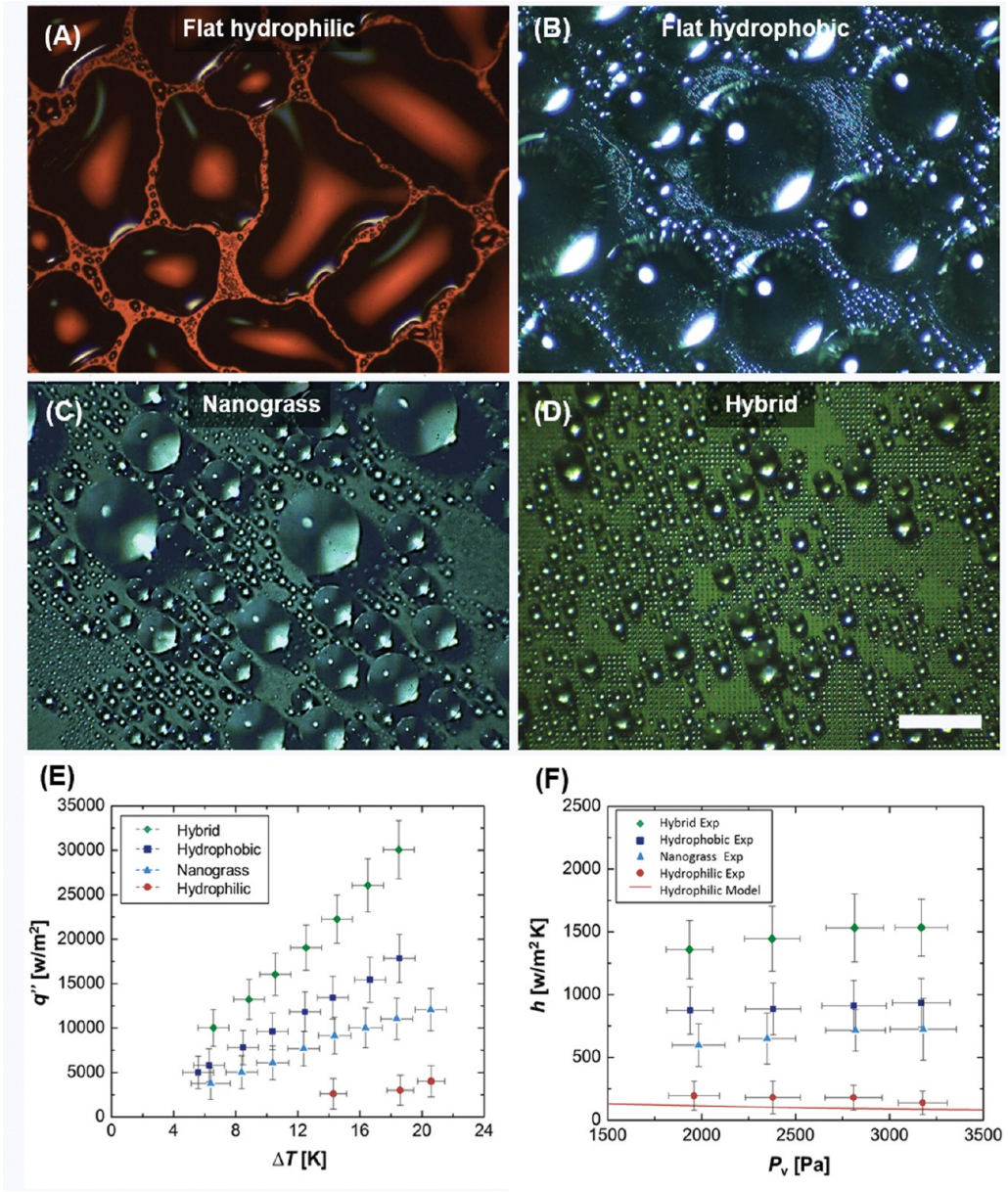

Figure 6. Heat transfer measurement. The condensation during thermal measurements was recorded using a high-speed camera on (A) flat hydrophilic, (B) flat hydrophobic, (C) nanograssed superhydrophobic surface, and (D) hybrid surface (scale bar, 300 μm). (E) Steady-state overall surface heat flux q'' as a function of subcooling ΔT for different condensing surfaces, undergoing filmwise, dropwise, and hybrid-wetting modes (hybrid surface design S/D = 2). (F) Steady-state condensation coefficient h as a function of the partial pressure of saturated vapor P_v for different condensing surfaces. Error bars indicate the propagation of the measurement errors associated with the temperatures of bulk gas, substrate back, and heat sink, as well as the humidity measurement.

As expected, the intensified nucleation density, fast droplet growth and departure rates naturally led to a larger surface coverage of small drops (as shown in Figure 5C), and the hybrid surface with S/D = 2 had the highest percentage (~69%) of droplets with diameter smaller than 10 μm. These results confirm our hypothesis on the synergistic cooperation for enhanced condensation, which is enabled by the combination of the filmwise and dropwise condensation through the wetting contrast of hydrophilic and superhydrophobic patterns.

Overall Heat Transfer Measurement. After qualifying the microscopic condensation characteristics including the initial growth rate, size distribution, and self-removal rate, we measured the macroscopic heat transfer coefficient. Figure 6A–D shows the snapshot images of condensation on various surfaces, *e.g.*, the flat hydrophilic, flat hydrophobic, superhydrophobic nanograss, and hybrid surfaces. The overall condensation heat transfer performance on these surfaces was measured in the condensation chamber (see Methods). Figure 6E shows the total heat flux q'' as a function of the temperature difference ΔT between the saturation vapor and condensed surface for these samples, at the partial pressure of vapor P_v = 2800 ± 146 Pa.

The overall heat transfer coefficient (HTC) was obtained from the slope of the curves shown in Figure 6E. On the flat hydrophilic surface with SiO_2 layer (Figure 6A), vapor quickly condensed and formed a water film that covered the entire surface. The HTC of the hydrophilic surface (180 ± 98 W/m^2·K) was the worst among the four surfaces because of the high thermal resistance of the unmovable liquid film. In contrast, for a flat hydrophobic surface, the discrete condensed droplets were shed by gravity and the surface was cleared out for renucleation, resulting in an improved HTC (939 ± 188 W/m^2·K). The superhydrophobic nanograssed surface, however, showed a 35% degradation of HTC (605 ± 165 W/m^2·K) compared to that of the flat hydrophobic surface. As we previously discussed, the gas layer beneath the condensed droplets significantly hinders the heat transfer rate and leads to the thermal degradation, despite more droplets of small size (~10−50 μm) appear on the nanograssed surface. Meanwhile, for a surface with homogeneous superhydrophobicity, the concave structures of nanograss can also lead to the formation of liquid bridge,[65] which greatly increases the droplet pinning force and thus can prevent coalesced droplet departure.[47] As shown in Figure 6C, some immobile droplets inevitably form during the condensation and gradually grow up to a large size (~300 μm). This immobile droplet coalescence caused by liquid bridges further degrade the heat transfer performance on the nanograssed surface during a prolonged condensation period. Figure 6D clearly shows the improvement of droplet nucleation density and size distribution on the hybrid surface. The spatial control of droplet condensation *via* the heterogeneous wettability efficiently avoids the liquid bridge formation, and subsequently reduces the number of immobile droplets on condensing surface. Therefore, it results in the highest heat transfer performance in the experiments, representing a 63% larger overall HTC (1532 ± 272 W/m^2·K) than that of the flat hydrophobic surface. The effect of partial vapor pressure on the overall thermal performance was also investigated. Figure 6F shows the overall HTC, h, as a function of the partial pressure of water vapor P_v in the condensation chamber. Note that the lower HTC relative to those achieved under pure vapor condition,[23,26] is mainly originated from the high concentration of noncondensable gas (NCG) in our experiments, which dramatically stunts the vapor diffusion to the condensing surface.[66] To verify the accuracy of our measurement data, we further compared our results on the hydrophilic and nanograssed surfaces with prior similar studies.[67−70] The data show reasonable agreement with literature values of the condensation HTC (~117 W/m^2·K for filmwise condensation and ~2000 W/m^2·K for jumping condensation). The theoretical model for filmwise condensation in the presence of NCG (red line) also agrees well with the experiments (red symbols) (see Supporting Information Note 5). According to the thermal characterization, the enhancement in HTC obtained on the hybrid surface is consistent with the prediction from the parameters in microscopic observation.

DISCUSSION

As discussed previously, the combination of two distinct condensation modes into one architecture has conflicting requirements on the surface morphological and chemical properties. For example, a large fraction of hydrophilic patch increases the droplet nucleation density, while the droplet departure behavior is compromised. To gain further insight for the surface optimization to harness the combinatorial advantages in both filmwise and dropwise condensation, we proposed a simple figure of merit to quantify the competition between the droplet nucleation, growth rate as well as droplet self-propelling. The figure of merit is expressed as

$$E^* \sim \varphi \cdot f_c^* \cdot \Delta G^* \quad (1)$$

where φ is the fraction of the hydrophilic patches on the hybrid surface, whose value $\varphi = \pi D^2/S^2$, can be a reflection of the embryo density. f_c^* is the nondimensional droplet coalescence frequency, which determines the efficiency of the condensation transition from filmwise to dropwise, and ΔG^* is the nondimensional excess surface energy measuring the ability of the droplet self-departure upon coalescence. Specifically, the droplet coalescence frequency can be expressed by $f_c^* = 1/(\tau_c/\tau_{eq})$. Here, τ_c is the time of droplet coalescence at the metastable state (*i.e.*, $\theta = \theta_c$) and τ_{eq} is the time when the condensed droplet reaches its equilibrium state (*i.e.*, $\theta = \theta_{eq}$), serving as the time normalization factor. Specifically, θ_c is the coalescence contact angle, calculated as $\theta_c = \sin^{-1}[(S/D)^{-1}]$, and θ_{eq} is equal to 15° for the flat hydrophilic SiO_2 surface, which is calculated from the advancing and receding angles (see Supporting Information Notes 1 and 3). On the basis of the different corresponding contact angles, both τ_c and τ_{eq} can be calculated from the proposed CCL droplet growth model (Supporting Information Note 4). Similarly, ΔG^* is expressed as $\Delta G/G_{eq}$ by using the energy normalization, in which ΔG is the excess surface energy released upon droplet coalescence, and $G_{eq} = \gamma_{lg} \cdot A_{lg} + \gamma_{sl} \cdot A_{sl}$ is the total surface free energy at the equilibrium state (θ_{eq} = 15°).

To simplify the energy derivation, it is assumed that the coalescence occurs between two droplets on adjacent micropillars (see Supporting Information Note 3), and the droplet becomes completely dewetting upon coalescence. Thus, ΔG can be expressed as

$$\Delta G = 2G_c - G_c' - 2E_{vis} \quad (2)$$

where G_c and G_c' are the surface free energies of droplet before and after the coalescence, given by $G_c = \gamma_{lg} \cdot A_{lg} + \gamma_{sl} \cdot A_{sl}$ with the droplets at θ_c, and

$G_c' = \gamma_{lg} \cdot A_{lg}' + \gamma_{sl} \cdot A_{sg}'$ with the merged droplet at the completely detached state. A and A' are the interfacial surface areas before and after coalescence, γ is the interfacial energy density and the subscripts s, l, and g denote the solid, liquid, and gas phase, respectively. The viscous dissipation energy for each droplet E_{vis} is obtained as[71,72] $E_{vis} = 36\pi\mu(\gamma_{lg} r^3 \rho^{-1})^{1/2}$, where the droplet radius r is derived as $r = D/(2 \sin \theta)$. For the CCL droplet on a micropillar, the interfacial surface areas can be estimated as $A_{lg} = 2\pi r^2 (1 - \cos \theta)$, and $A_{sl} = \pi D^2/4$. For the merged droplet, the interfacial surface areas are $A_{lg}' = \pi S^2[(1 - \cos \theta_c)^2 \cdot (2 + \cos \theta_c)/2]^{2/3}$ and $A_{sg}' = 2A_{sl}$, respectively.

As presented above, the droplet nucleation, coalescence frequency and induced departure driven energy are dependent on the morphological parameters such as the diameter of the hydrophilic patch D, the center-to-center spacing of micropillars S, and the wetting properties of the hybrid patterns. In Figure 7, we plot the figure of merit, E^*, as a function of S/D. The optimal S/D where the maximum E^* occurs is between 2 and 3. This optimal S/D may be attributed to the competing factors among φ, f_c^*, and ΔG^* in eq 1. For a hybrid surface with smaller S/D, the droplet nucleation density φ and coalescence frequency f_c^* are relatively larger. However, the fast droplet coalescence of these dense droplets accordingly leads to a smaller released energy ΔG^*; therefore, the figure of merit is undermined. By contrast, for a hybrid surface with a larger S/D, due to the large spacing between the individual droplets localized in the hydrophilic patches, the droplet coalescence f_c^* is suppressed, though the released energy is relatively large (see Supporting Information Note 4). Thus, the figure of merit is small as well. Note that for varying diameters of the hydrophilic patches (D = 1, 6, and 10 μm), the optimal S/D for E^* is similar (see Supporting Information Note 5). The hybrid surface can lose the benefit of filmwise to dropwise transition when the hydrophilic patch is too large (D > 10 μm). The condensed liquid fails to form droplets in a rapid manner on an oversized hydrophilic area, and becomes immobile due to the large contact line pinning force (see Supporting Information Movie 2). Although we only consider the two-droplet coalescence in our model, the analysis shows excellent agreement with the experimental data (Figure 5). Therefore, the analysis of E^* in the model we developed provides a reasonable prediction for the surface optimization.

Note that in our model, we did not consider the electrostatic charging of jumping droplets during condensation, which has received increasing attention recently.[73−75] On the hybrid surface, although the majority of droplets contact the hydrophilic SiO_2 area rather than the hydrophobic coating, we suspect that the jumping droplets would be positively charged due to the electric double layer formed between the droplets and SiO_2 surface, which possesses a negative zeta potential similar to most fluoropolymer coatings. This hypothesis will be validated in our future work *via* the characterization of jumping droplets on the hybrid surface in the electric-field assisted condensation, and the potential of further enhancing condensation heat transfer on the hybrid surfaces using electric fields will also be investigated.

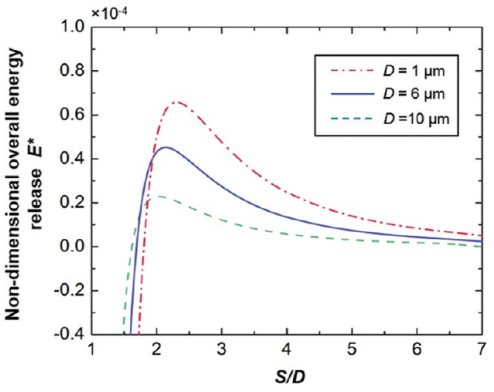

Figure 7. Surface optimization. Plot of the figure of merit E^* as a function of the ratio of the center-to-center space to the diameter of the micropillar S/D. Here E^* is defined as the nondimensional overall energy release for evaluating the synergetic effects of combined filmwise and dropwise condensation, indicating the competition between the embryo nucleation density, coalescence frequency, and droplet self-propelling. The maximum E^* occurs at S/D ranging between 2 and 3. If S/D is too small or big, E^* is compromised.

CONCLUSIONS

To summarize, we reported a novel strategy that allowed for the mutual reinforcement of two condensation modes. By wisely implementing the high wetting contrast inspired by the natural beetle shell, our hybrid surface reconciles the conflicts encountered in filmwise and dropwise condensation in conventional designs. We also proposed an analytical model that provided important insight for the optimization of the morphological features. The measured heat transfer coefficient of the optimized hybrid surface demonstrated a 63% enhancement as compared to the conventional dropwise condensation on the flat hydrophobic silicon surface. We believe our novel surface can also be extended for many other promising applications such as water harvesting, desalination, and anti-icing.[76,77]

METHODS

Fabrication Procedure of the Hybrid Nanostructured Surface. A 525 μm thick silicon wafer coated with 1 μm silicon oxide coating was used in the experiments. First, the silicon oxide layer was patterned using standard photolithography, followed by advanced oxide dry etching. The resulted silicon oxide pattern

served as a mask for wet etching of silicon. Next, the micropillars were etched briefly in tetramethylammonium hydroxide (TMAH) solution. Excess SiO_2 rim on the top of the micropillars due to the undercutting of TMAH etching was removed by a second photolithography and oxide dry etching. Then the modified Bosch deep reactive ion etching (DRIE) process was used to fabricate uniform nanopillars on the sidewalls and in the spaces between the micropillars. The DRIE process included cyclic passivation and etching modes in which C_4F_8 and SF_6 were used as the reactants, respectively. In this study, the inductively coupled plasma DRIE system (Surface Technology Systems, U.K.) was used as the etcher. The coil power was set at ~550 W. The chamber pressure and temperature was kept at ~25 mTorr and ~20 °C. In the passivation cycle, the C_4F_8 flow rate was ~85 sccm. In the etching cycle, the SF_6 flow rate was ~70 sccm and platen power was set at ~15 W. At the end of DRIE process, a thin film of hydrophobic fluoride polymer was deposited on the nanpillars to achieve the global superhydrophobicity, whereas the fluoride polymer on the top of SiO_2 was selectively removed by immersing in buffered oxide etchant for ~120 s to form the hydrophilic spots on the surface. The dimension of the micropillars is ~6 μm in diameter, ~7 μm in height and the center-to-center distance varies from 12 to 24 μm. The nanopillars with diameter of ~200 nm, height of ~5 μm, and pitch of ~400−800 nm were fabricated using 20 DRIE processing cycles. The advancing and receding contact angles were measured on the as-fabricated hybrid surface, flat SiO_2, fluorinated flat silicon, and fluorinated silicon nanograssed surfaces (see Supporting Information Table S2).

Condensation Characterization Using ESEM. Condensation nucleation and growth were studied on these fabricated surfaces using an environmental scanning electron microscope (Philips XL-30). The sample substrate was placed on a stainless steel sample holder with a tilt angle of ~45° on a Peltier cooling stage to observe growth dynamics and wetting morphologies. A gaseous secondary electron detector was employed for imaging. The electron beam voltage was set at ~15 keV in order to ensure the better contrast for image visualization as well as limiting droplet heating effect.[78] The condensation process can be triggered by precisely controlling the stage temperature and the water vapor pressure in the chamber. The temperature of the Peltier cooling stage was fixed at ~0.3 °C. The water vapor pressure was gradually increased to ~4.9 Torr, resulting in the nucleation of water droplets on the sample surface from the saturated water vapor, and then maintained at ~4.8 Torr during imaging.

Condensation Imaging and Thermal Characterization in Custom-Made Chamber. Droplet growth behavior was studied using a custom-made chamber. The supplied gas that consisted of saturated water vapor and a high fraction of pure nitrogen simulated the working condition of the cooling systems in dehumidification and water harvesting applications. The vapor was generated from a sealed chamber by injecting N_2 into a temperature-controlled water reservoir. The partial pressure of saturation vapor varied from ~1.93 to ~3.17 kPa, corresponding to saturation vapor temperatures of 17−25 °C. The tested samples were mounted in the condensation chamber, in which the relative humidity and temperature of the bulk gas were continuously monitored by a humidity probe (HX94C, Omega) and thermocouples (TJ36-CAIN-032U-6, Omega). The temperature gradient of the copper heat sink was measured by an array of thermocouples to determine the condensation heat flux. The heat released from condensation on the test surface was removed by a cooling loop connected with a thermostatic water bath. A flow meter (S-114, McMillan) with an accuracy of ±1.0% was integrated at the inlet to monitor the flow rate in the cooling loop. The hydraulic diameter of the flow path was 7 mm, and the flow rate of cooling water was set at 2 L/min in all experiments. By controlling the cooling water temperature, the condensation subcooling was adjusted from 6 to 20 °C, extrapolated from the temperature measurement (CHAL-003-BW, Omega) taken at the backside of the substrate. The data was recorded using the National Instruments NI-9214 thermocouple module. Rapid evolution of droplet nucleation, growth and departure was recorded using a high speed camera (Phantom v7.3, Vision Research).

Conflict of Interest: The authors declare no competing financial interest.

Supporting Information Available: Four videos showing the filmwise-to-dropwise transition, spatial control and coalesce-induced droplet jumping on hybrid surfaces, as well as further information on hybrid wettability verification, droplet growth model, droplet wetting and coalescence dynamics, evolution of droplet adhesion, supplementary analysis of figure-of-merit for condensation performance on hybrid surface and filmwise condensation model with NCG. This material is available free of charge *via* the Internet at http://pubs.acs.org.

Acknowledgment. We gratefully acknowledge financial support from The Hong Kong University of Science and Technology under Grant No. FSGRF12EG52 and RGC General Research Fund No. 621110 to S.Y., and RGC General Research Fund No.125312 and City University of Hong Kong Strategic Research Grants No.7004076 to Z.W. S.Y., Z.W., and Y.H. conceived the research. S.Y. and Z.W. supervised the research. Y.H. designed and carried out the sample fabrication and condensation experiments. X.C. and Y.H. carried out the ESEM observation. Y.H., X.C., and M.Y. analyzed the data. Y.H. and M.Y. developed the model. S.Y., Z.W., and Y.H. wrote the manuscript.

REFERENCES AND NOTES

1. Boreyko, J. B.; Chen, C.-H. Vapor Chambers with Jumping-Drop Liquid Return from Superhydrophobic Condensers. *Int. J. Heat Mass Transfer* **2013**, *61*, 409–418.
2. Dietz, C.; Rykaczewski, K.; Fedorov, A. G.; Joshi, Y. Visualization of Droplet Departure on a Superhydrophobic Surface and Implications to Heat Transfer Enhancement During Dropwise Condensation. *Appl. Phys. Lett.* **2010**, *97*, 033104.
3. Dehbi, A.; Guentay, S. A Model for the Performance of a Vertical Tube Condenser in the Presence of Noncondensable Gases. *Nucl. Eng. Des.* **1997**, *177*, 41–52.
4. Khawaji, A. D.; Kutubkhanah, I. K.; Wie, J.-M. Advances in Seawater Desalination Technologies. *Desalination* **2008**, *221*, 47–69.
5. Humplik, T.; Lee, J.; O'Hern, S.; Fellman, B.; Baig, M.; Hassan, S.; Atieh, M.; Rahman, F.; Laoui, T.; Karnik, R. Nanostructured Materials for Water Desalination. *Nanotechnology* **2011**, *22*, 292001.
6. Beysens, D. Dew Nucleation and Growth. *C. R. Phys.* **2006**, *7*, 1082–1100.
7. Rykaczewski, K.; Scott, J. H. J.; Rajauria, S.; Chinn, J.; Chinn, A. M.; Jones, W. Three Dimensional Aspects of Droplet Coalescence During Dropwise Condensation on Superhydrophobic Surfaces. *Soft Matter* **2011**, *7*, 8749–8752.
8. Lee, A.; Moon, M.-W.; Lim, H.; Kim, W.-D.; Kim, H.-Y. Water Harvest *via* Dewing. *Langmuir* **2012**, *28*, 10183–10191.
9. Daniel, S.; Chaudhury, M. K.; Chen, J. C. Fast Drop Movements Resulting from the Phase Change on a Gradient Surface. *Science* **2001**, *291*, 633–636.
10. Liu, Y.; Moevius, L.; Xu, X.; Qian, T.; Yeomans, J. M.; Wang, Z. Pancake Bouncing on Superhydrophobic Surfaces. *Nat. Phys.* **2014**, *10*, 515–519.
11. Boreyko, J. B.; Chen, C. H. Self-Propelled Dropwise Condensate on Superhydrophobic Surfaces. *Phys. Rev. Lett.* **2009**, *103*, 184501.
12. Rykaczewski, K.; Osborn, W. A.; Chinn, J.; Walker, M. L.; Scott, J. H. J.; Jones, W.; Hao, C. L.; Yao, S. H.; Wang, Z. K. How Nanorough Is Rough Enough to Make a Surface Superhydrophobic During Water Condensation? *Soft Matter* **2012**, *8*, 8786–8794.
13. Feng, J.; Qin, Z. Q.; Yao, S. H. Factors Affecting the Spontaneous Motion of Condensate Drops on Superhydrophobic Copper Surfaces. *Langmuir* **2012**, *28*, 6067–6075.
14. Wisdom, K. M.; Watson, J. A.; Qu, X.; Liu, F.; Watson, G. S.; Chen, C.-H. Self-Cleaning of Superhydrophobic Surfaces by Self-Propelled Jumping Condensate. *Proc. Natl. Acad. Sci. U.S.A.* **2013**, *110*, 7992–7997.
15. Mikic, B. On Mechanism of Dropwise Condensation. *Int. J. Heat Mass Transfer* **1969**, *12*, 1311–1323.

16. Kim, S.; Kim, K. J. Dropwise Condensation Modeling Suitable for Superhydrophobic Surfaces. *J. Heat Transfer* **2011**, *133*, 081502–1–081502–7.
17. Dimitrakopoulos, P.; Higdon, J. On the Gravitational Displacement of Three-Dimensional Fluid Droplets from Inclined Solid Surfaces. *J. Fluid Mech.* **1999**, *395*, 181–209.
18. Rose, J. Dropwise Condensation Theory and Experiment: A Review. *Proc. Inst. Mech. Eng., Part A* **2002**, *216*, 115–128.
19. Kim, H.-Y.; Lee, H. J.; Kang, B. H. Sliding of Liquid Drops Down an Inclined Solid Surface. *J. Colloid Interface Sci.* **2002**, *247*, 372–380.
20. Tian, J.; Zhu, J.; Guo, H.-Y.; Li, J.; Feng, X.-Q.; Gao, X. Efficient Self-Propelling of Small-Scale Condensed Microdrops by Closely Packed ZnO Nanoneedles. *J. Phys. Chem. Lett.* **2014**, *5*, 2084–2088.
21. Bocquet, L.; Lauga, E. A Smooth Future? *Nat. Mater.* **2011**, *10*, 334–337.
22. Paxson, A. T.; Yagüe, J. L.; Gleason, K. K.; Varanasi, K. K. Stable Dropwise Condensation for Enhancing Heat Transfer *via* the Initiated Chemical Vapor Deposition (iCVD) of Grafted Polymer Films. *Adv. Mater.* **2014**, *26*, 418–423.
23. Miljkovic, N.; Enright, R.; Nam, Y.; Lopez, K.; Dou, N.; Sack, J.; Wang, E. N. Jumping-Droplet-Enhanced Condensation on Scalable Superhydrophobic Nanostructured Surfaces. *Nano Lett.* **2012**, *13*, 179–187.
24. Rafiee, J.; Mi, X.; Gullapalli, H.; Thomas, A. V.; Yavari, F.; Shi, Y.; Ajayan, P. M.; Koratkar, N. A. Wetting Transparency of Graphene. *Nat. Mater.* **2012**, *11*, 217–222.
25. Anderson, D. M.; Gupta, M. K.; Voevodin, A. A.; Hunter, C. N.; Putnam, S. A.; Tsukruk, V. V.; Fedorov, A. G. Using Amphiphilic Nanostructures to Enable Long-Range Ensemble Coalescence and Surface Rejuvenation in Dropwise Condensation. *ACS Nano* **2012**, *6*, 3262–3268.
26. Cheng, J. T.; Vandadi, A.; Chen, C. L. Condensation Heat Transfer on Two-Tier Superhydrophobic Surfaces. *Appl. Phys. Lett.* **2012**, *101*, 131909.
27. Torresin, D.; Tiwari, M. K.; Del Col, D.; Poulikakos, D. Flow Condensation on Copper-Based Nanotextured Superhydrophobic Surfaces. *Langmuir* **2012**, *29*, 840–848.
28. He, M.; Zhang, Q.; Zeng, X.; Cui, D.; Chen, J.; Li, H.; Wang, J.; Song, Y. Hierarchical Porous Surface for Efficiently Controlling Microdroplets' Self-Removal. *Adv. Mater.* **2013**, *25*, 2291–2295.
29. Lo, C. W.; Wang, C. C.; Lu, M. C. Spatial Control of Heterogeneous Nucleation on the Superhydrophobic Nanowire Array. *Adv. Funct. Mater.* **2013**, *24*, 1211–1217.
30. Chen, X.; Ma, R.; Zhou, H.; Zhou, X.; Che, L.; Yao, S.; Wang, Z. Activating the Microscale Edge Effect in a Hierarchical Surface for Frosting Suppression and Defrosting Promotion. *Sci. Rep.* **2013**, *3*, 2515.
31. Xiao, R.; Miljkovic, N.; Enright, R.; Wang, E. N. Immersion Condensation on Oil-Infused Heterogeneous Surfaces for Enhanced Heat Transfer. *Sci. Rep.* **2013**, *3*, 1988.
32. Liu, T.; Sun, W.; Sun, X.; Ai, H. Thermodynamic Analysis of the Effect of the Hierarchical Architecture of a Superhydrophobic Surface on a Condensed Drop State. *Langmuir* **2010**, *26*, 14835–14841.
33. Azimi, G.; Dhiman, R.; Kwon, H.-M.; Paxson, A. T.; Varanasi, K. K. Hydrophobicity of Rare-Earth Oxide Ceramics. *Nat. Mater.* **2013**, *12*, 315–320.
34. Chen, X. M.; Wu, J.; Ma, R. Y.; Hua, M.; Koratkar, N.; Yao, S. H.; Wang, Z. K. Nanograssed Micropyramidal Architectures for Continuous Dropwise Condensation. *Adv. Funct. Mater.* **2011**, *21*, 4617–4623.
35. Zhang, T.; Wang, J.; Chen, L.; Zhai, J.; Song, Y.; Jiang, L. High-Temperature Wetting Transition on Micro- and Nanostructured Surfaces. *Angew. Chem., Int. Ed.* **2011**, *50*, 5311–5314.
36. Kashchiev, D. *Nucleation: Basic Theory with Applications*, 1st ed.; Butterworth-Heinemann: Oxford, 2000.
37. Carey, V. P. *Liquid-Vapor Phase-Change Phenomena: An Introduction to the Thermophysics of Vaporization and Condensation Processes in Heat Transfer Equipment*, 2nd ed.; Taylor & Francis: London, 2007.
38. Varanasi, K. K.; Hsu, M.; Bhate, N.; Yang, W. S.; Deng, T. Spatial Control in the Heterogeneous Nucleation of Water. *Appl. Phys. Lett.* **2009**, *95*, 094101.
39. Miljkovic, N.; Enright, R.; Wang, E. N. Effect of Droplet Morphology on Growth Dynamics and Heat Transfer During Condensation on Superhydrophobic Nanostructured Surfaces. *ACS Nano* **2012**, *6*, 1776–1785.
40. Moulinet, S.; Bartolo, D. Life and Death of a Fakir Droplet: Impalement Transitions on Superhydrophobic Surfaces. *Eur. Phys. J. E* **2007**, *24*, 251–260.
41. Bormashenko, E.; Bormashenko, Y.; Stein, T.; Whyman, G.; Pogreb, R.; Barkay, Z. Environmental Scanning Electron Microscopy Study of the Fine Structure of the Triple Line and Cassie-Wenzel Wetting Transition for Sessile Drops Deposited on Rough Polymer Substrates. *Langmuir* **2007**, *23*, 4378–4382.
42. Wang, J.; Chen, D. Criteria for Entrapped Gas under a Drop on an Ultrahydrophobic Surface. *Langmuir* **2008**, *24*, 10174–10180.
43. Patankar, N. A. Transition between Superhydrophobic States on Rough Surfaces. *Langmuir* **2004**, *20*, 7097–7102.
44. Patankar, N. A. Consolidation of Hydrophobic Transition Criteria by Using an Approximate Energy Minimization Approach. *Langmuir* **2010**, *26*, 8941–8945.
45. Lafuma, A.; Quere, D. Superhydrophobic States. *Nat. Mater.* **2003**, *2*, 457–460.
46. Enright, R.; Miljkovic, N.; Al-Obeidi, A.; Thompson, C. V.; Wang, E. N. Condensation on Superhydrophobic Surfaces: The Role of Local Energy Barriers and Structure Length Scale. *Langmuir* **2012**, *28*, 14424–14432.
47. Rykaczewski, K.; Paxson, A. T.; Anand, S.; Chen, X.; Wang, Z.; Varanasi, K. K. Multimode Multidrop Serial Coalescence Effects During Condensation on Hierarchical Superhydrophobic Surfaces. *Langmuir* **2012**, *29*, 881–891.
48. Dorrer, C.; Ruhe, J. Some Thoughts on Superhydrophobic Wetting. *Soft Matter* **2009**, *5*, 51–61.
49. Neelesh, A. P. Supernucleating Surfaces for Nucleate Boiling and Dropwise Condensation Heat Transfer. *Soft Matter* **2010**, *6*, 1613–1620.
50. Graham, C.; Griffith, P. Drop Size Distributions and Heat Transfer in Dropwise Condensation. *Int. J. Heat Mass Transfer* **1973**, *16*, 337–346.
51. Rykaczewski, K. Microdroplet Growth Mechanism During Water Condensation on Superhydrophobic Surfaces. *Langmuir* **2012**, *28*, 7720–7729.
52. Yao, C.-W.; Alvarado, J. L.; Marsh, C. P.; Jones, B. G.; Collins, M. K. Wetting Behavior on Hybrid Surfaces with Hydrophobic and Hydrophilic Properties. *Appl. Surf. Sci.* **2014**, *290*, 59–65.
53. Parker, A. R.; Lawrence, C. R. Water Capture by a Desert Beetle. *Nature* **2001**, *414*, 33–34.
54. Mishchenko, L.; Khan, M.; Aizenberg, J.; Hatton, B. D. Spatial Control of Condensation and Freezing on Superhydrophobic Surfaces with Hydrophilic Patches. *Adv. Funct. Mater.* **2013**, *23*, 4577–4584.
55. Volmer, M.; Weber, A. Nucleus Formation in Supersaturated Systems. *Z. Phys. Chem. (Leipzig)* **1926**, *119*, 277–301.
56. Oliver, J.; Huh, C.; Mason, S. Resistance to Spreading of Liquids by Sharp Edges. *J. Colloid Interface Sci.* **1977**, *59*, 568–581.
57. Zhai, L.; Berg, M. C.; Cebeci, F. C.; Kim, Y.; Milwid, J. M.; Rubner, M. F.; Cohen, R. E. Patterned Superhydrophobic Surfaces: Toward a Synthetic Mimic of the Namib Desert Beetle. *Nano Lett.* **2006**, *6*, 1213–1217.
58. Quéré, D. Wetting and Roughness. *Annu. Rev. Mater. Res.* **2008**, *38*, 71–99.
59. Miljkovic, N.; Enright, R.; Wang, E. N. Modeling and Optimization of Superhydrophobic Condensation. *J. Heat Transfer* **2013**, *135*, 111004–111004.
60. Boreyko, J. B.; Zhao, Y.; Chen, C.-H. Planar Jumping-Drop Thermal Diodes. *Appl. Phys. Lett.* **2011**, *99*, 234105.
61. Miljkovic, N.; Wang, E. N. Condensation Heat Transfer on Superhydrophobic Surfaces. *MRS Bull.* **2013**, *38*, 397–406.
62. Enright, R.; Miljkovic, N.; Alvarado, J. L.; Kim, K.; Rose, J. W. Dropwise Condensation on Micro- and Nanostructured

Surfaces. *Nanoscale Microscale Thermophys. Eng.* **2014**, *18*, 223–250.
63. Tuteja, A.; Choi, W.; Ma, M.; Mabry, J. M.; Mazzella, S. A.; Rutledge, G. C.; McKinley, G. H.; Cohen, R. E. Designing Superoleophobic Surfaces. *Science* **2007**, *318*, 1618–1622.
64. Mayama, H.; Nonomura, Y. Theoretical Consideration of Wetting on a Cylindrical Pillar Defect: Pinning Energy and Penetrating Phenomena. *Langmuir* **2011**, *27*, 3550–3560.
65. Rykaczewski, K.; Landin, T.; Walker, M. L.; Scott, J. H. J.; Varanasi, K. K. Direct Imaging of Complex Nano- to Microscale Interfaces Involving Solid, Liquid, and Gas Phases. *ACS Nano* **2012**, *6*, 9326–9334.
66. Castillo, J. E.; Weibel, J. A.; Garimella, S. V. The Effect of Relative Humidity on Dropwise Condensation Dynamics. *Int. J. Heat Mass Transfer* **2015**, *80*, 759–766.
67. Ölçeroğlu, E.; Hsieh, C.-Y.; Rahman, M. M.; Lau, K. K. S.; McCarthy, M. Full-Field Dynamic Characterization of Superhydrophobic Condensation on Biotemplated Nanostructured Surfaces. *Langmuir* **2014**, *30*, 7556–7566.
68. Peterson, P. Theoretical Basis for the Uchida Correlation for Condensation in Reactor Containments. *Nucl. Eng. Des.* **1996**, *162*, 301–306.
69. Herranz, L. E.; Anderson, M. H.; Corradini, M. L. A Diffusion Layer Model for Steam Condensation within the Ap600 Containment. *Nucl. Eng. Des.* **1998**, *183*, 133–150.
70. Ganguli, A.; Patel, A.; Maheshwari, N.; Pandit, A. Theoretical Modeling of Condensation of Steam Outside Different Vertical Geometries (Tube, Flat Plates) in the Presence of Noncondensable Gases Like Air and Helium. *Nucl. Eng. Des.* **2008**, *238*, 2328–2340.
71. Chandra, S.; Avedisian, C. T. On the Collision of a Droplet with a Solid Surface. *Proc. R. Soc. London, Ser. A* **1991**, *432*, 13–41.
72. Wang, F.-C.; Yang, F.; Zhao, Y.-P. Size Effect on the Coalescence-Induced Self-Propelled Droplet. *Appl. Phys. Lett.* **2011**, *98*, 053112.
73. Miljkovic, N.; Preston, D. J.; Enright, R.; Wang, E. N. Electrostatic Charging of Jumping Droplets. *Nat. Commun.* **2013**, *4*, 2517.
74. Miljkovic, N.; Preston, D. J.; Enright, R.; Wang, E. N. Electric-Field-Enhanced Condensation on Superhydrophobic Nanostructured Surfaces. *ACS Nano* **2013**, *7*, 11043–11054.
75. Miljkovic, N.; Preston, D. J.; Enright, R.; Wang, E. N. Jumping-Droplet Electrostatic Energy Harvesting. *Appl. Phys. Lett.* **2014**, *105*, 013111.
76. Jung, S.; Tiwari, M. K.; Doan, N. V.; Poulikakos, D. Mechanism of Supercooled Droplet Freezing on Surfaces. *Nat. Commun.* **2012**, *3*, 615.
77. Maitra, T.; Tiwari, M. K.; Antonini, C.; Schoch, P.; Jung, S.; Eberle, P.; Poulikakos, D. On the Nanoengineering of Superhydrophobic and Impalement Resistant Surface Textures Below the Freezing Temperature. *Nano Lett.* **2013**, *14*, 172–182.
78. Rykaczewski, K.; Scott, J. H. J.; Fedorov, A. G. Electron Beam Heating Effects During Environmental Scanning Electron Microscopy Imaging of Water Condensation on Superhydrophobic Surfaces. *Appl. Phys. Lett.* **2011**, *98*, 093106.